iScience

CellPress
OPEN ACCESS

Article

Striatal direct pathway neurons play leading roles in accelerating rotarod motor skill learning

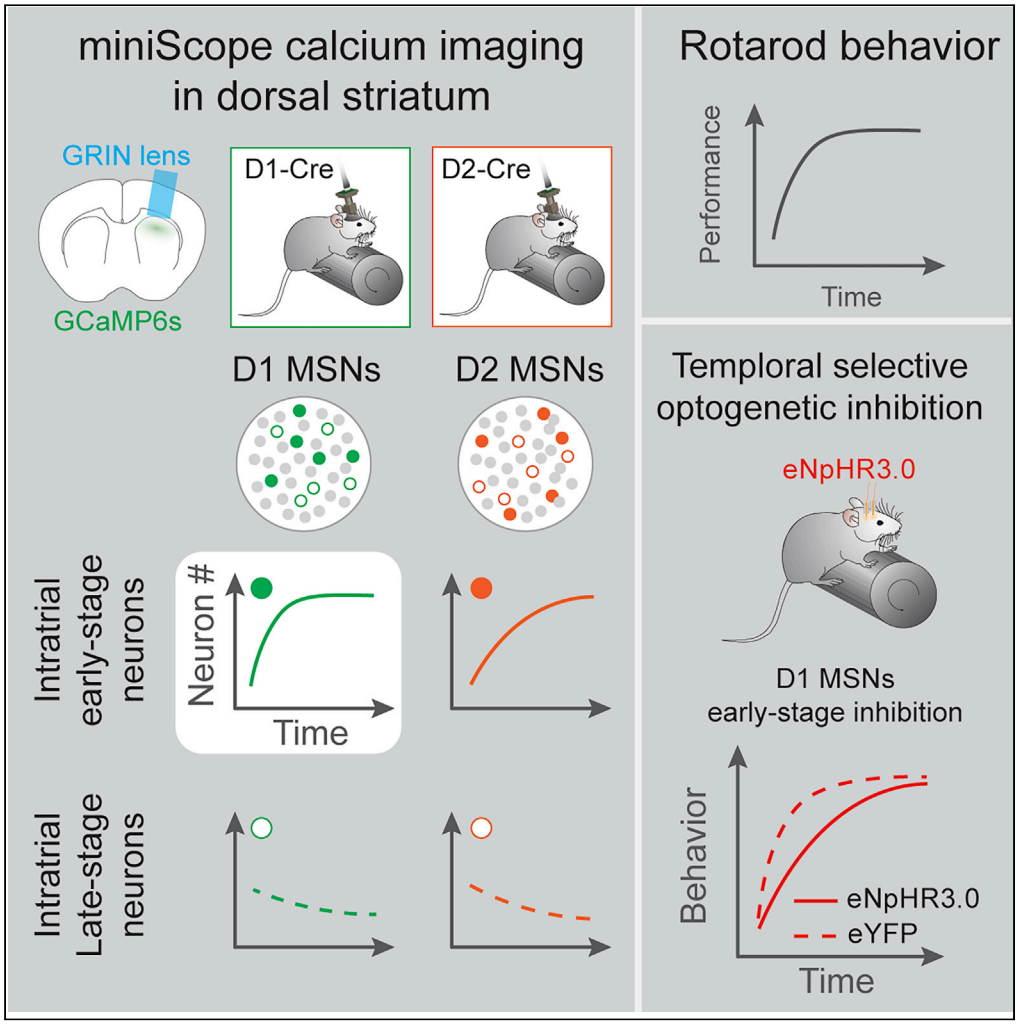

Bo Liang, Lifeng Zhang, Yan Zhang, ..., Charles R. Gerfen, Giovanni Barbera, Da-Ting Lin

da-ting.lin@nih.gov (D.-T.L.)
giovanni.barbera@nih.gov (G.B.)

Highlights

Distinct subsets of D1 and D2 MSNs correlate with different behavioral variables

Intratrial early-stage D1 MSNs correlates with rotarod motor skill learning

Speed coding in dorsal striatum is stable across rotarod training

Optogenetic inhibition of early-stage D1 MSNs impairs rotarod motor skill learning

Liang et al., iScience 25, 104245
May 20, 2022
https://doi.org/10.1016/j.isci.2022.104245

iScience

CellPress
OPEN ACCESS

Article

Striatal direct pathway neurons play leading roles in accelerating rotarod motor skill learning

Bo Liang,[1,2,7] Lifeng Zhang,[1,7] Yan Zhang,[1] Craig T. Werner,[1] Nicholas J. Beacher,[1] Alex J. Denman,[1] Yun Li,[3] Rong Chen,[4] Charles R. Gerfen,[5] Giovanni Barbera,[1,*] and Da-Ting Lin[1,6,8,*]

SUMMARY

Dorsal striatum is important for movement control and motor skill learning. However, it remains unclear how the spatially and temporally distributed striatal medium spiny neuron (MSN) activity in the direct and indirect pathways (D1 and D2 MSNs, respectively) encodes motor skill learning. Combining miniature fluorescence microscopy with an accelerating rotarod procedure, we identified two distinct MSN subpopulations involved in accelerating rotarod learning. In both D1 and D2 MSNs, we observed neurons that displayed activity tuned to acceleration during early stages of trials, as well as movement speed during late stages of trials. We found a distinct evolution trajectory for early-stage neurons during motor skill learning, with the evolution of D1 MSNs correlating strongly with performance improvement. Importantly, optogenetic inhibition of the early-stage neural activity in D1 MSNs, but not D2 MSNs, impaired accelerating rotarod learning. Together, this study provides insight into striatal D1 and D2 MSNs encoding motor skill learning.

INTRODUCTION

Striatal medium spiny neurons (MSNs) of the direct (D1 MSNs) and indirect pathways (D2 MSNs) in the basal ganglia play important yet complex roles in motor behaviors (Barbera et al., 2016; Costa et al., 2004; Cui et al., 2013; Gritton et al., 2019; Jin et al., 2014; Klaus et al., 2017; Kravitz et al., 2010; Parker et al., 2018; Santos et al., 2015; Tecuapetla et al., 2014; Yin et al., 2009; Yttri and Dudman, 2016), including motor skill learning (Costa et al., 2004; Jin et al., 2014; Kupferschmidt et al., 2017; Santos et al., 2015). Increasing evidence (Barbera et al., 2016; Cui et al., 2013; Klaus et al., 2017; Kupferschmidt et al., 2017; Parker et al., 2018) suggests that the rate of striatal MSN activity, MSN spatiotemporal profiles, and local circuits is crucial to striatal function. Yet, neural correlates of striatal MSNs over the course of motor skill learning remain to be determined. Here we asked how the spatially and temporally distributed activity of the direct and indirect pathway MSNs are engaged during motor skill learning. We employed a miniature fluorescence microscope system to record *in vivo* calcium activity from MSNs in the dorsal striatum longitudinally while mice trained on the accelerating rotarod task. We identified two subpopulations in both direct and indirect pathway MSNs: "intratrial early-stage" neurons that displayed an elevated activity early in each trial and was negatively and non-linearly correlated with rotarod speed, and "intratrial late-stage" neurons that displayed activity positively and linearly tuned to rotarod speed. Importantly, the evolution of intratrial early-stage neurons in D1 MSNs was better correlated with the improvement in rotarod task performance, indicating a more prominent role for D1 MSNs in motor skill learning. We also found that optogenetic inhibition of the early-stage activity of D1, but not D2, MSNs impaired accelerating rotarod motor skill learning. Together, this study provides insight into differential engagement of D1 and D2 MSNs in motor skill learning.

RESULTS

Neural correlates of motor skill learning in D1 and D2 MSNs

The striatum is important for motor skill learning, and thought to guide movement by outputting to motor thalamus topographically *via* the GPi "direct" pathway, comprising of MSNs expressing dopamine D1 receptors (D1 MSNs) (Gerfen et al., 1990), or the GPe "indirect" pathway, comprising of MSNs expressing dopamine D2 receptors (D2 MSNs) (Gerfen et al., 1990). To understand the role of striatal D1 and D2

[1]Intramural Research Program, National Institute on Drug Abuse, National Institutes of Health, 333 Cassell Drive, Baltimore, MD 21224, USA

[2]School of Electrical Engineering & Computer Science, College of Engineering & Mines, University of North Dakota, Grand Forks, ND 58202, USA

[3]Department of Zoology and Physiology, University of Wyoming, 1000 E University Avenue, Laramie, WY 82071, USA

[4]Department of Diagnostic Radiology and Nuclear Medicine, University of Maryland School of Medicine, 100 N Greene St, Baltimore, MD 21201, USA

[5]Intramural Research Program, National Institute of Mental Health, National Institutes of Health, Building 49, Room 5A60, Bethesda, MD 20814, USA

[6]The Solomon H. Snyder Department of Neuroscience, Johns Hopkins University School of Medicine, 725 N. Wolfe Street, Baltimore, MD 21205, USA

[7]These authors contribute equally

[8]Lead contact

*Correspondence: da-ting.lin@nih.gov (D.-T.L.), giovanni.barbera@nih.gov (G.B.)

https://doi.org/10.1016/j.isci.2022.104245

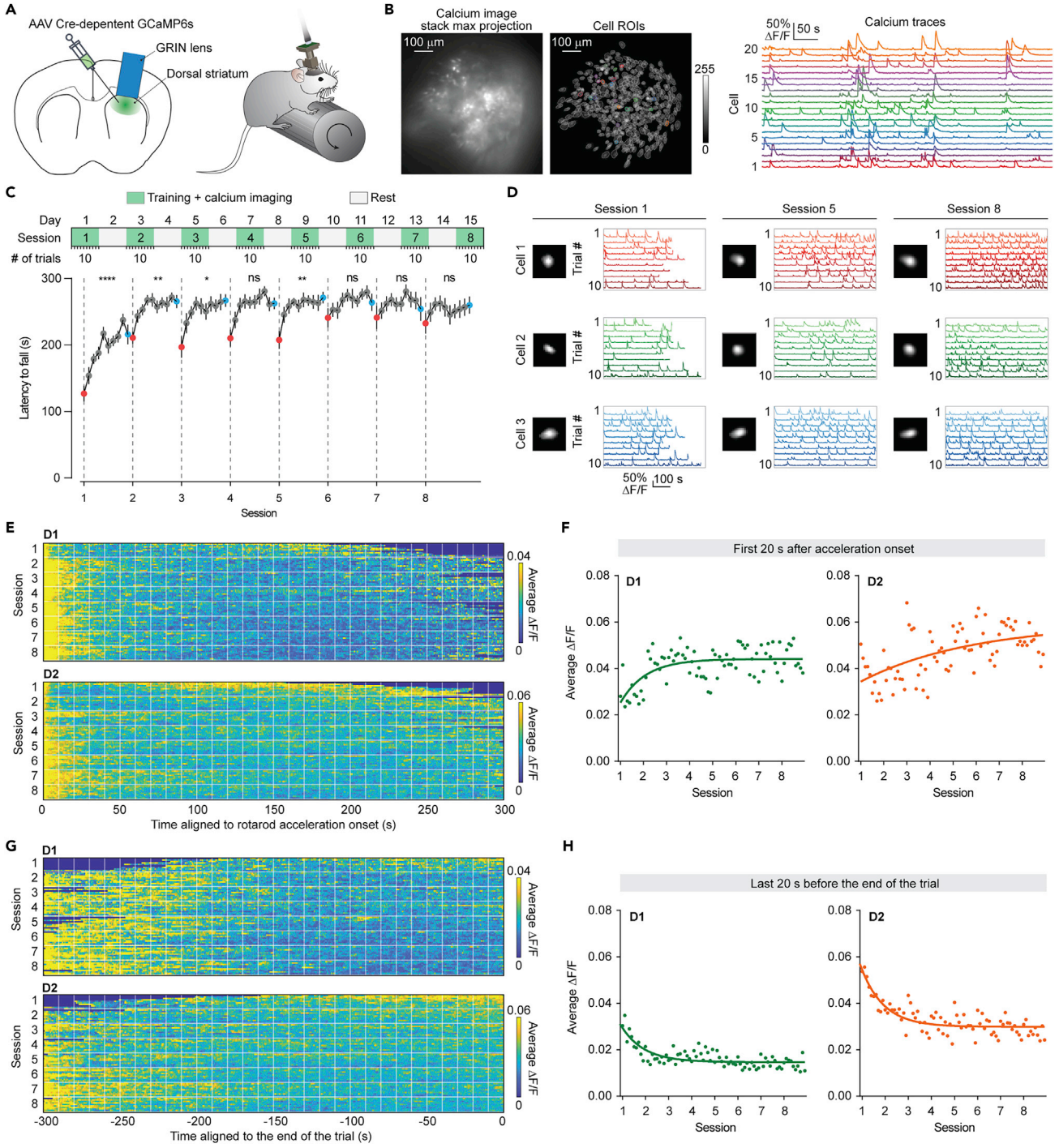

Figure 1. Engagements of D1 and D2 MSNs in dorsal striatum over two-week rotarod training

(A) Left: schematic of GRIN lens implanted in dorsal striatum; right: rotarod motor skill learning task while the mouse carries a miniature microscope for calcium imaging.

(B) Left: representative maximum projection calcium image of D2 MSNs labeled with GCaMP6s from a D2-Cre mouse; middle: regions of interest of cells detected using the CaImAn method; right: representative calcium traces from 21 regions of interest (color-matched with the left ROIs).

(C) Top: experimental timeline; bottom: latency to fall off the rotarod over two-week rotarod training (n = 15 mice). Red and blue dots: the first and last trial in each session.

(D) Cell footprints and calcium traces of 10 trials from three representative cells in three sessions.

(E) Raster plots of average calcium activity of all neurons from all mice during each trial over eight sessions. For each trial, calcium traces were aligned to the onset of rotarod acceleration. Top: average calcium activity of D1-Cre mice (n = 9); bottom: average calcium activity of D2-Cre mice (n = 6).

Figure 1. *Continued*

(F) Plots of the average calcium activity from D1 (left) and D2 mice (right) during the initial 20 s after the onset of rotarod acceleration for all 80 trials. Dots represent the mean value and traces indicate the curve fitting results using one phase decay.

(G) Raster plots of average calcium activity of all neurons from all mice during each trial over eight sessions. For each trial, calcium traces were aligned to the end of the trial. Top: average calcium activity of D1-Cre mice (n = 9); Bottom: average calcium activity of D2-Cre mice (n = 6).

(H) Plots of the average calcium activity from D1 (left) and D2 mice (right) during the last 20 s before the end of each trial.

Dots represent the mean value from all mice and traces indicate the curve fitting results using one phase decay.*p < 0.05; **p < 0.01; ***p < 0.001; ****p < 0.0001; ns, not significant (p > 0.05). Data points indicate the mean; Error bars indicate SEM.

See also Figures S1–S3 and Table S1.

MSNs in motor skill learning, we combined the accelerating rotarod motor skill learning procedure (Jones and Roberts, 1968; Lalonde et al., 1995) with miniScope calcium imaging (Barbera et al., 2016; Zhang et al., 2019) (Figures 1A and 1B; Figures S1 and S2; STAR Methods). We trained and imaged mice for 10 trials per session, every day, for a total of eight training sessions (Figure 1C; Video S1). Evidenced by a longer latency to fall, mice displayed fast learning in session 1, slow learning from session 2 to 5, and stable performance from session 6 to 8 (Figure 1C; see all statistical results in Table S1). We extracted calcium traces of individual neurons in each session (Figure 1D; STAR methods) (Giovannucci et al., 2019; Pnevmatikakis et al., 2016; Zhou et al., 2018), and registered neurons across days based on the distance and similarity of their spatial footprints (Figure 1D; Figure S3; STAR methods) (Sheintuch et al., 2017).

We observed that both D1 and D2 MSNs displayed elevated population activity in both the early and late stages of each trial (Figures 1E and 1G). To study the activity during the early stage of the trial, we aligned calcium traces to rotarod acceleration onset (Figure 1E). We then calculated average activity in the first 20 s of each trial (denoted as early-stage). Both D1 and D2 MSNs showed an elevated early-stage activity that decreased as the trial progressed and the rotarod accelerated (Figure 1F). D1 MSNs displayed the prominent intratrial early-stage activity from session 2 onward (Figure 1F left panel), whereas D2 MSNs showed a slower progression of an increased intratrial early-stage activity (Figure 1F right panel).

The length of each trial was dependent on the rotarod performance (i.e., latency to fall). To study the activity during the late stage of the trial (denoted as late-stage, last 20 s), we aligned calcium traces to the end of each trial (Figure 1G). In contrast to the increased intratrial early-stage activity across learning, the intratrial late-stage activity decreased across learning. In the first session, both D1 and D2 MSNs displayed an increased intratrial late-stage activity before the end of each trial, with a more prominent D2 MSNs increase (Figure 1H). In addition, the intratrial late-stage activity from D1 MSNs showed a trend of faster decay compared with D2 MSNs across learning (Figure 1H; Table S1). Together, these results show greater engagement of D1 MSNs and slower evolution of D2 MSNs across accelerating rotarod learning, indicating distinct roles of D1 and D2 MSNs in accelerating rotarod motor skill learning.

Intratrial early- and late-stage neurons are distinct subpopulations

We next examined neural correlates of accelerating rotarod motor skill learning at the single neuron level. We first calculated Spearman's correlation coefficients between the activity of individual neurons and rotarod speed using 10-s bins (STAR Methods). We identified both D1 and D2 neurons whose activity was positively or negatively correlated with rotarod speed (Figure 2A; STAR Methods). We defined these neurons as either intratrial early-stage neurons (whose activity non-linearly and negatively correlated with rotarod speed within-trials; see Figure 3A) or intratrial late-stage neurons (whose activity linearly and positively correlated with rotarod speed within-trials; see Figure 3B). For both D1 and D2 MSNs, the percentage of intratrial late-stage neurons slightly decreased across training, whereas the percentage of intratrial early-stage neurons increased across training (Figures 2B and 2C). Importantly, the percentage of intratrial early-stage neurons, but not intratrial late-stage neurons, correlated with the subject's behavioral performance across learning in both D1 and D2 MSNs (Figures 2B and 2C; Table S1). For D1 MSNs, the rate of increase in intratrial early-stage neurons was greater for D2 MSNs (Table S1), whereas the rates of decrease in intratrial late-stage neurons were similar for D1 and D2 MSNs (Table S1). These results suggest that intratrial early-stage neurons represent neural correlates of accelerating rotarod motor skill learning, and that neural correlates with accelerating rotarod motor skill learning emerge first from D1 MSNs and subsequently from D2 MSNs.

We reasoned that if the intratrial early-stage neurons among D1 and D2 MSNs represent neural correlates of accelerating rotarod motor skill learning, the evolution of other characteristics of these neurons should also correlate with the subject's behavioral performance. First, we evaluated how consistently neurons were

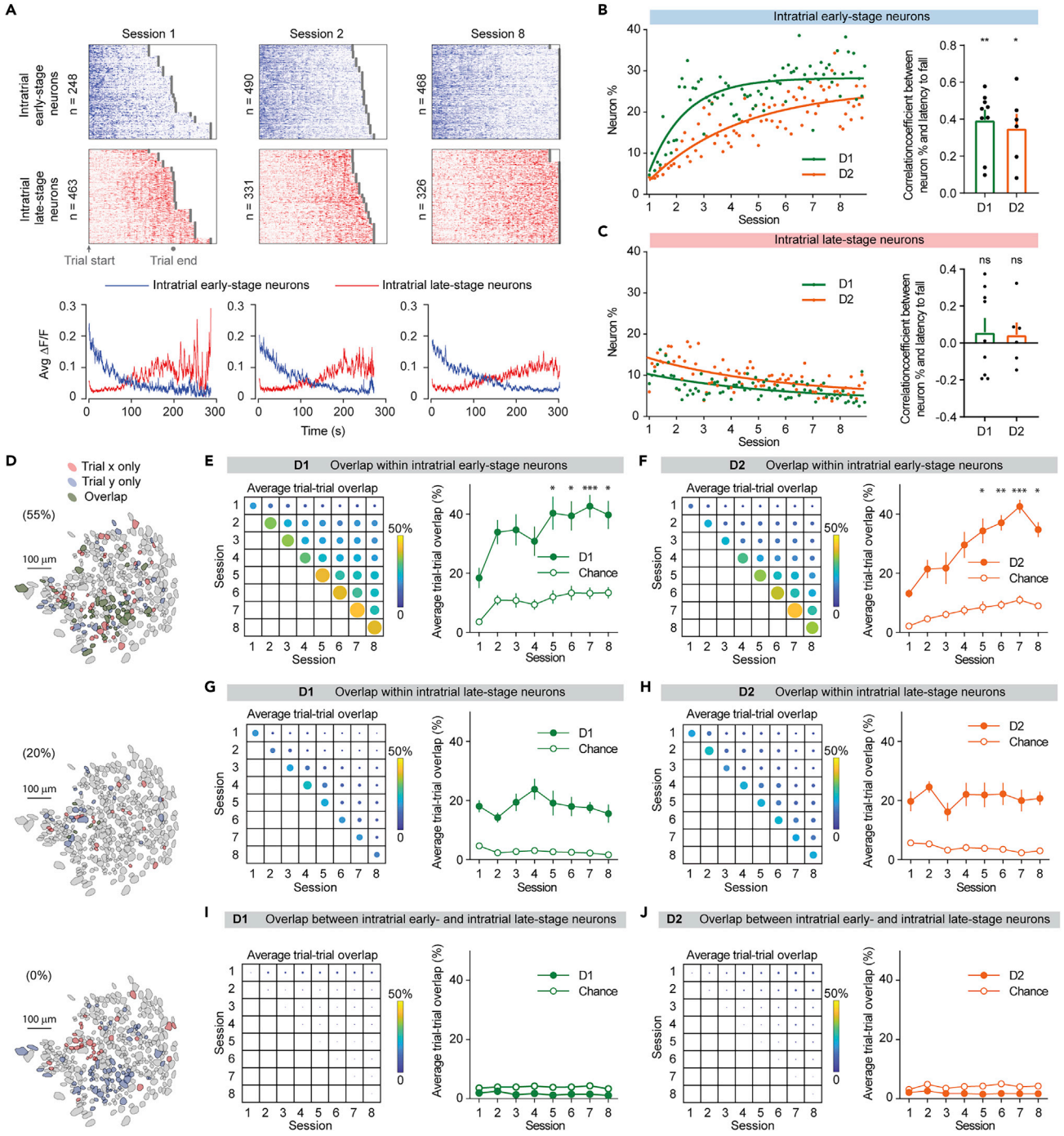

Figure 2. Intratrial early- and late-stage neurons belong to distinct subpopulations

(A) Comparisons of intratrial early- and late-stage neurons from a representative mouse at sessions 1, 2, and 8. Top row: raster plots of individual calcium activity from intratrial early-stage neurons identified during each session; middle row: raster plot of individual calcium activity from intratrial late-stage neurons identified during each session; bottom row: average calcium traces from all identified intratrial early- (blue traces) and late-stage (red traces) neurons.

(B) Left: changes in neural numbers for early-stage neurons across eight sessions, from D1-Cre (Green) and D2-Cre (Orange) mice. Traces indicate the curve fitting results using exponential plateau. Right: correlation coefficients between neuron number changes and behavioral performance (i.e., latency to fall) for intratrial early-stage neurons. Dots indicate correlation coefficient average from individual mouse, and histogram bars indicate the mean value of all mice.

(C) Left: changes in neural numbers for intratrial late-stage neurons across eight sessions, from D1-Cre (Green) and D2-Cre (Orange) mice. Traces indicate the curve fitting results using one phase decay. Right: correlation coefficients between neuron number changes and behavioral performance (i.e., latency to

Figure 2. *Continued*

fall) for intratrial late-stage neurons. Dots indicate correlation coefficient average from individual mouse, and histogram bars indicate the mean value of all mice.

(D) Representative cell maps showing different levels of overlaps between identified neural ensembles. Top: overlap of the intratrial early-stage neural ensembles identified at two trials in a session, displays an ~55% overlapping ratio. Middle: overlap of the intratrial late-stage neural ensembles identified at two trials in a session, displays an ~20% overlapping ratio. Bottom: overlap between intratrial early- and late-stage neural ensembles identified at two trials in a session, displays an ~0% overlapping ratio.

(E and F) Left matrix: trial-to-trial cell overlaps between intratrial early-stage neural ensembles identified at any two sessions for D1 (E) and D2 MSNs (F). Right trace: quantification of the averaged trial-to-trial cell overlaps (solid dots) within each session and those predicted by chance (open dots).

(G and H) Trial-to-trial cell overlap analysis between intratrial late-stage neural ensembles identified at different sessions. All other legends are similar to (E and F).

(I and J) Trial-to-trial cell overlap analysis between intratrial early- and late-stage neural ensembles identified at different sessions.

All other legends are similar to (E and F). *$p < 0.05$; **$p < 0.01$; ***$p < 0.001$; ns, not significant ($p > 0.05$). Error bars indicate SEM.

See also Table S1.

identified as either intratrial early- or late-stage neurons. We calculated the average trial-to-trial cell overlap between any two training sessions (Figure 2D; see STAR Methods). Three types of cell overlap were calculated: overlap within intratrial early-stage neurons (Figures 2E and 2F), overlap within intratrial late-stage neurons (Figures 2G and 2H), and overlap between intratrial early- and late-stage neurons (Figures 2I and 2J). Within a given session, for intratrial early-stage neurons, the trial-to-trial cell overlap increased with training and sustained at ~40% in later training sessions (Figures 2E and 2F; Table S1), coinciding with a plateau in behavioral performance (Figure 1C), whereas the trial-to-trial cell overlap for intratrial late-stage neurons was maintained near 20% across rotarod training (higher than that predicted by chance; Figures 2G and 2H). In contrast, the cell overlap between intratrial early- and late-stage neurons was close to zero and below the chance level under all circumstances (Figures 2I and 2J). These findings suggest that specific organizational strategies may prevent the recruitment of the same neurons into intratrial early and late-stage neural populations.

Speed coding in dorsal striatum is stable across rotarod training

We found that activity profiles and evolution patterns of intratrial early- and late-stage neurons were markedly different across rotarod training. We calculated the average calcium activity in 10-s bins of intratrial early- (Figure 3A) and late-stage neurons (Figure 3B) for all trials of every session. We found similar patterns for both D1 and D2 MSNs; the intratrial early-stage neuron activity was exponentially related to rotarod speed and similar across training (Figure 3A right panel), whereas the intratrial late-stage neuron activity was linearly tuned to the rotarod speed (Figure 3B right panel). Particularly, for the first session, the average trial activity decreased with training (Figures 3A and 3B left panel) and was markedly higher during session 1 when compared with later sessions (Figures 3A and 3B right panel). This result suggests that striatal coding of speed and accelerating rotarod motor skill learning is mediated by distinct neural mechanisms.

Striatal activity encodes speed information during movement (Gerfen et al., 1990). Therefore, one potential neural mechanism in accelerating rotarod motor skill learning is better prediction of rotarod speed *via* training, which would allow mice to remain on the accelerating rotarod for longer durations of time. We tested whether speed decoding using the activity of D1 and D2 MSNs improved across rotarod training. We trained gradient boosting machine (GBM; see STAR Methods) models using a subset of calcium activity from all detected cells and rotarod speed data, and subsequently tested the performance for speed decoding using the rest of calcium activity data (Figure 3C). We evaluated the speed decoding performance by calculating the Pearson's correlation coefficient between the observed and predicted speed. We found that the decoding performance using D2 MSN activity was higher than dthat using D1 MSN activity (Figure 3D), likely owing to the relatively higher activity level of D2 MSNs in the accelerating rotarod task (Figures 1F and 1H). Surprisingly, for both D1 and D2 MSNs, the speed decoding performance was similar across the rotarod training, suggesting that learning on an accelerating rotarod may have a different neural basis from speed monitoring and control in the dorsal striatum.

Intratrial early-stage optogenetic inhibition of D1, but not D2, MSNs activity impaired accelerating rotarod motor skill learning

Our imaging data revealed that the intratrial early-stage activity of D1 MSNs better correlated with rotarod performance (Figures 1 and 2). To determine whether the intratrial early-stage activity of D1 MSNs plays a causal role in accelerating rotarod motor skill learning, we employed optogenetics to specifically inhibit intratrial early- or late-stage MSN activity in the accelerating rotarod task (da Silva et al., 2018; Panigrahi

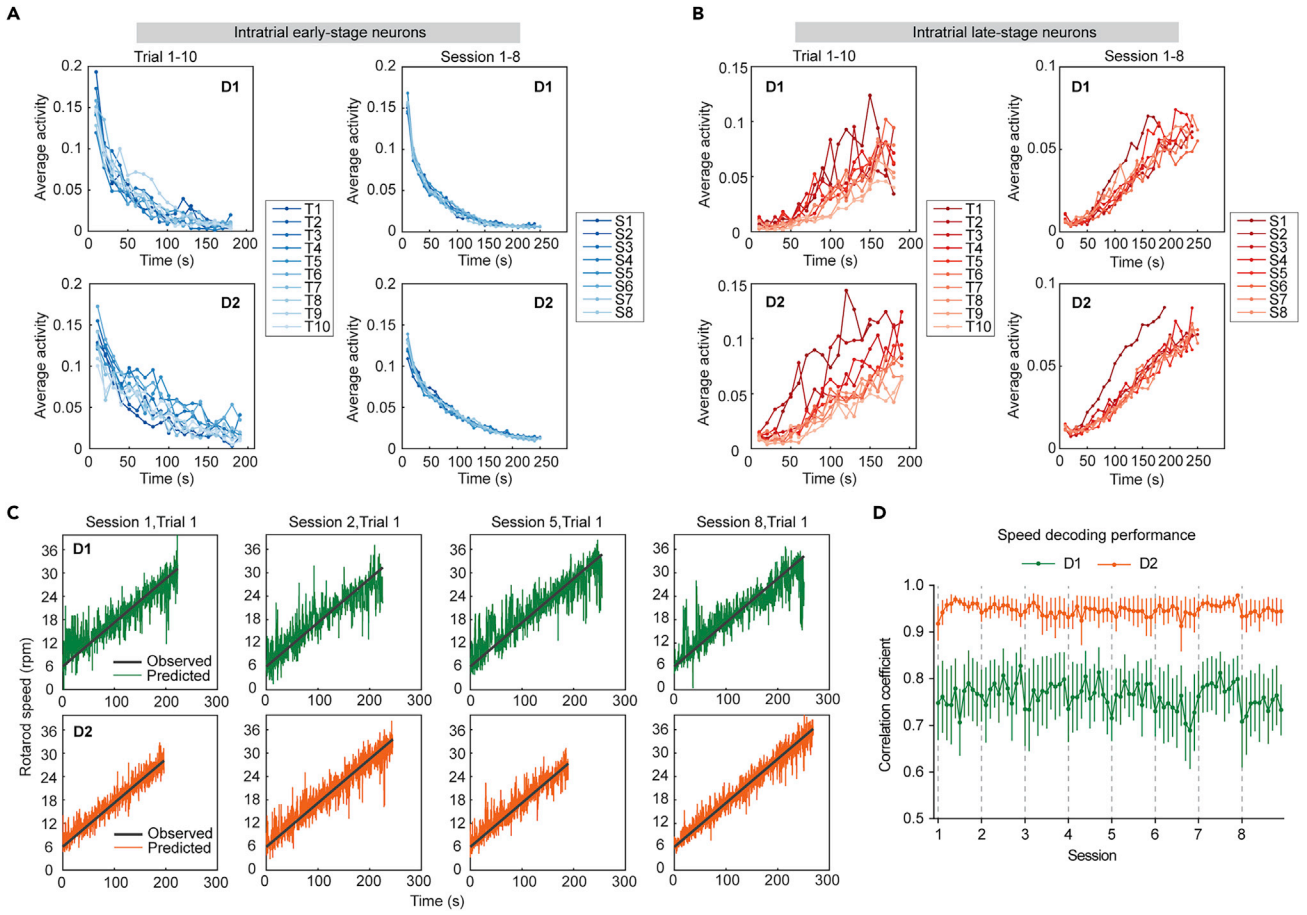

Figure 3. Speed decoding performance is stable across rotarod training

(A) Left panels: average calcium activity of intratrial early-stage neurons at each trial of the first training session (session 1); right panels: average calcium activity of intratrial early-stage neurons at each session. Top: D1 MSNs; bottom: D2 MSNs.

(B) Similar to (A), panels show the average calcium activity of intratrial late-stage neurons at each trial of session 1 (left) and across all sessions (right).

(C) Representative examples of the actual and the predicted speed based on the calcium activity during trials of different sessions. Green: D1 MSNs; orange: D2 MSNs.

(D) Correlation coefficients between the actual speed and the predicted speed for D1 (green) and D2 (orange) MSNs. Error bars indicate SEM.

See also Table S1.

et al., 2015). To determine if we can inhibit MSN activity using eNpHR3.0, we first developed a dual-LED miniScope prototype, which allows us to perform combined calcium imaging and eNpHR3.0 inhibition of MSNs simultaneously in freely moving mice (Figure S4A, STAR Methods). We mixed AAV encoding Cre-dependent GCaMP7f and AAV encoding Cre-dependent eNpHR3.0-iRFP (Richie et al., 2017) and injected them into the dorsal striatum of either D1- or D2-Cre mice. We then implanted GRIN lens into dorsal striatum unilaterally, and imaged GCaMP7f in the absence or presence of lime LED turning on (566–569 nm peak wavelength) that activates eNpHR3.0. Our results showed that compared with lime LED OFF, lime LED ON resulted in suppression of both D1- and D2-MSN activity (Figures S4B–S4D). Whereas the degree of inhibition is moderate, likely owing to the low lime LED intensity in this dual LED prototype miniscope (approximately 60 μW measured at the bottom of miniScope, STAR Methods), these results clearly show that MSN activity can be inhibited using eNpHR3.0 *in vivo*.

To inhibit the activity of D1 or D2 MSNs on the accelerating rotarod task, we injected AAV encoding Cre-dependent eNpHR3.0-EYFP bilaterally into the dorsal striatum of either D1- or D2-Cre mice. We then bilaterally implanted optical fibers above the viral injection sites (Figures 4A, S4E and S4F). We then trained mice in the same accelerating rotarod task (Figure 4B) used for the calcium imaging experiment. For intratrial early-stage optogenetic inhibition (Figure 4C), we turned on the 568-nm laser (approximately 10 mW

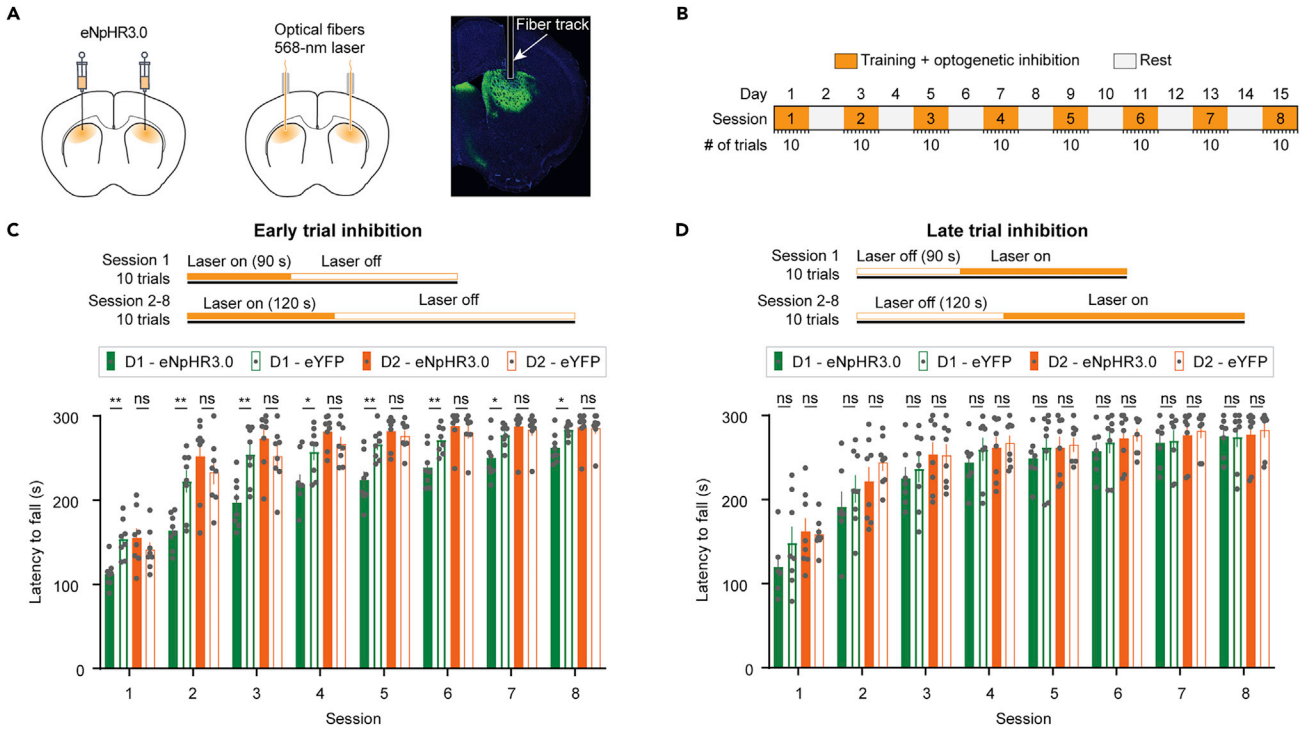

Figure 4. Optogenetic inhibition of intratrial early-stage D1 MSNs, but not D2 MSNs, impairs rotarod motor skill learning

(A) Schematic of neuron labelling (left) and optical fiber implantation (middle) for optogenetic inhibition experiment. Right histological image shows the implanted optical fiber track in the dorsal striatum.

(B) Timeline of the optogenetic experiment.

(C) Top: schematic of early inhibition strategy; bottom: rotarod behavioral performance with optogenetic inhibition of D1 (green) or D2 (orange) MSNs during the early stage of trials.

(D) Similar to (C) but for optogenetic inhibition during the late stage of trials.*$p < 0.05$; **$p < 0.01$; ns, not significant ($p > 0.05$). Error bars indicate SEM. See also Figure S4 and Table S1.

measured at each fiber tip) only in the early stage of a trial (session 1: 90 s; sessions 2–8: 120 s from the trial acceleration onset) to target the activity of intratrial early-stage neurons. For intratrial late-stage neuron optogenetic inhibition (Figure 4D), we turned on the 568-nm laser only during the late-stage segment of a trial (session 1: 90 s; sessions 2–8: 120 s after the trial acceleration onset). Consistently, D1 and D2 control groups showed similar behavior performance (Figure S4H). The overall inhibition durations were similar among early and late inhibition groups (Figure S4G). We found that intratrial early-stage optogenetic inhibition of D1, but not D2, MSN activity impaired improvement in acceleratingthe rotarod performance at all stages of training (Figure 4C; Table S1). Intratrial late-stage optogenetic inhibition of D1 or D2 MSN activity had no effect on improvement in accelerating the rotarod performance (Figure 4D; Table S1). Together, our optogenetic inhibition experiments suggest that the intratrial early-stage activity of D1 MSNs plays more prominent roles in the accelerating rotarod motor skill learning. These findings were consistent with results from our calcium imaging experiments, in which the evolution of intratrial early-stage D1 MSNs is better correlated with the improvement in accelerating the rotarod performance.

DISCUSSION

Our results from both calcium imaging and optogenetics indicate a leading role of D1 MSNs in accelerating rotarod motor skill learning. From our optogenetic experiments, we note that the mice in which intratrial early-stage D1 MSNs were inhibited still showed improvement in their performance across trials. Mice were able to learn the task toward the end of training, but the overall rate of learning was lower compared with that of the control group (Figure 4). These findings indicate that other neurons in the striatum are likely involved in rotarod motor skill learning and performance. This interpretation is supported by previous studies where fast spiking interneurons have been shown to be important for motor control (Gittis et al., 2011; Gritton et al., 2019), habitual operant behavior (O'Hare et al., 2017), and learning of new behaviors

(Lee et al., 2017; Martiros et al., 2018; Owen et al., 2018). Neurons in other brain regions may also play important roles in rotarod motor skill learning. It is also possible that the intratrial early-stage neurons may be related to somatosensory stimulation associated with postural adjustments and random movements/sensory stimulation (Carelli et al., 1997; Cho and West, 1997; Mittler et al., 1994; Tang et al., 2007, 2009), which decrease naturally when animals are forced to run at a higher speed. Indeed, studies showed that dorsal striatal D1 and D2 neurons respond to both passive and active stimulation of single body parts (Coffey et al., 2016, 2017) and have been shown to receive input from somatosensory and motor areas of cortex (Bolam et al., 2000). As such, it is theorized that the dorsal striatum is modulated by ascending spiral-projection patterns within the limbic system (Haber et al., 2000) and it is likely that somatosensory-related cues influence learning processes in order to refine cognitively advanced technical aspects of motor skills. It has also been proposed that neurons in the dorsal striatum exist to refine ongoing movements (Coffey et al., 2017), and using motor skills necessary to run on an accelerating rotarod involves processing and recognizing somatosensory cues related to both the initial change in acceleration (intratrial early stage) and maintenance of speed (intratrial late stage) to achieve success. Therefore, it is likely that both phases of motor skill practice require synchronous and non-competitive processing in order to promote effective skill learning.

Our data also support the notion that dorsal striatum plays an important role in monitoring movement speed. The existence of speed correlated neural activity in the dorsal striatum was reported in several studies using electrophysiology and calcium imaging methods in MSNs (Barbera et al., 2016; Bartholomew et al., 2016; Costa et al., 2004; Cui et al., 2013; Kim et al., 2014; Parker et al., 2018; Rueda-Orozco and Robbe, 2015; Sales-Carbonell et al., 2018; Yttri and Dudman, 2016), interneurons (Gritton et al., 2019), and axon projections from midbrain dopamine neurons (Howe and Dombeck, 2016). Recent works also revealed a "continuous encoding model" (Fobbs et al., 2020) or "moment-to-moment movement monitoring model" (Sales-Carbonell et al., 2018) on the role of striatal activity in relation to movement, consistent with our observations that striatal D1 and D2 MSNs have heterogeneous relationships to the rotarod speed (Figures 2 and 3). Early in training, there are ~10% of D1 and D2 MSNs whose activity monotonically increased with the increasing rotarod speed, subsequently decreased to ~5% over extended training, and population activity also followed a parallel trend of reduction (Figure 2), even though the average intratrial late-stage rotarod speed increased as the behavior performance improved. These results suggest that for both D1 and D2 MSNs, the intratrial late-stage activity becomes less necessary during well-trained sessions, indicating that in addition to speed monitoring, the intratrial late-stage activity of D1 and D2 MSNs may also represent a certain internal state that reflects movement efforts or motivation (Panigrahi et al., 2015; Yttri and Dudman, 2016). Another possible explanation could be that dorsal striatum receives projections from other brain regions, such as the cerebellum (Xiao et al., 2018) or midbrain (Howe and Dombeck, 2016; Panigrahi et al., 2015), which represent movement kinetic information, and learning may lead to a transition from higher dependency between these brain regions early in training to a regime of autonomous function after learning is completed. Further investigation of this may require simultaneous recordings of dorsal striatum and other brain regions that project to the dorsal striatum. It is worth noting that optogenetic inhibition of the intratrial late-stage activity did not impair the improvement in accelerating rotarod learning (Figure 4). Given the previous optogenetic inhibition studies (Panigrahi et al., 2015), our data do not necessarily imply that these intratrial late-stage activities are unnecessary for motor skill learning. More sophisticated behavior procedures, such as gait or stepping analysis (Cao et al., 2015), may provide more insights into how D1 and D2 MSNs regulate speed control during motor skill learning.

Several recent studies (Nonomura et al., 2018; Sheng et al., 2019; Shin et al., 2018; Tecuapetla et al., 2014) suggest that the direct pathway facilitates the intended action and the indirect pathway inhibits the unintended action. For example, Tecuapetla et al. showed that enhancing the activity of D1 MSNs sustained the performance of learned sequences, whereas enhancing the activity of D2 MSNs aborted ongoing performance (Tecuapetla et al., 2014). Geddes et al. also demonstrated that stimulation of D1 MSNs selectively inserts a single action element into an established action sequence, whereas the activation of D2 MSNs removes the ongoing subsequence while leaving the rest of the sequence intact (Geddes et al., 2018). Our data showed that D1 MSNs engaged early in training, whereas D2 MSN engage gradually across training (Figures 2 and 4). Our results, together with recent studies discussed above, raise an interesting possibility that direct pathway MSNs may code learned motor skill, whereas indirect pathway MSNs may prevent unintended movement to support the newly learning motor skills. More future experiments will be needed to test this possibility.

Limitations of the study

We acknowledge that there are several limitations of our study. First, the acceleration rotarod is a simple model of motor skill learning, and there are more complex features of motor skill learning that require more behaviorally advanced models to study. Therefore, it will be important to utilize different behavioral probes in future studies to better understand a neural activity that underlies finer detailed features of motor skill learning. Second, optogenetic inhibition of MSNs will not only inhibit the output of MSNs to downstream basal ganglia targets, but also local circuit effects of these neurons through intra-striatal collaterals (Burke et al., 2017). However, it is worth noting that D2 MSNs are more likely to form collaterals providing lateral inhibitions to D1 MSNs than vice versa (Dobbs et al., 2016; Planert et al., 2010; Taverna et al., 2008). In our optogenetic inhibition results, we only observed impairment of rotarod motor skill learning when we inhibited intratrial early-stage D1 MSNs. If the impairment in motor skill learning is through lateral inhibition from D1 to D2 MSNs (or D2 to D1 MSN inhibition), one would expect rotarod motor skill learning impairment when we inhibited the activity of intratrial early-stage D2 MSNs that we did not observe. Therefore, it is reasonable to rule out the possible contribution of lateral inhibition from D1 to D2 MSNs, and vice versa, in our optogenetic results. Third, whereas GCaMP6f has been shown to report single action potentials using two-photon imaging (Chen et al., 2013), we do not know under our miniScope imaging conditions if we can reliably observe single action potential. It is possible that most calcium transients we detected mainly reflect short firing bursts of MSNs, but this technical limitation should not affect the conclusions of this study. Finally, the use of D2-Cre mice rather than A2A-Cre mice may target a small number of interneurons among the D2 MSNs. From Gritton and colleagues' study (Gritton et al., 2019), the percentage of observed Parvalbumin (PV) and Cholinergic (CHI) interneurons could be ~3.5% relative to D2 MSNs (assuming the numbers of D1 and D2 MSNs are similar). It is important to note that in Gritten et al.'s study, PV neurons display a prolonged calcium activity, which we rarely observed in our D2 calcium imaging data. The number of CHI neurons is very small relative to that of D2 MSNs. Therefore, we believe that mistargeting the interneurons in D2-Cre mice is unlikely to affect the major conclusions of this study.

Together, our study leveraged miniScope imaging in an accelerating rotarod task to provide new insights into the roles of dorsal striatum D1 and D2 MSNs in motor skill learning.

STAR★METHODS

Detailed methods are provided in the online version of this paper and include the following:

- KEY RESOURCES TABLE
- RESOURCE AVAILABILITY
  - Lead contact
  - Materials availability
  - Data and code availability
- EXPERIMENTAL MODEL AND SUBJECT DETAILS
- METHOD DETAILS
  - Virus injection
  - GRIN lens and optical fiber implantation
  - Rotarod tasks
  - Calcium imaging using miniature microscope
  - Combined calcium imaging and optogenetics using dual LED miniScope prototype
  - Optogenetic experiments
  - Immunostaining
  - Calcium image processing
  - Cell registration across days
- QUANTIFICATION AND STATISTICAL ANALYSIS
  - Data analysis
  - Identification of intratrial early- and late-stage neurons in accelerating rotarod task
  - Speed decoding
  - Statistics
  - Sample size estimation

SUPPLEMENTAL INFORMATION

Supplemental information can be found online at https://doi.org/10.1016/j.isci.2022.104245.

ACKNOWLEDGMENTS

Research was supported by Intramural Research Program, National Institute on Drug Abuse, National Institutes of Health. Y.Z., N.J.B., and C.T.W. are supported by Postdoctoral Fellowship from the Center on Compulsive Behaviors, National Institutes of Health. Y.L. is supported by National Institutes of Health (NIH) grants 5P20GM121310, R61NS115161, and UG3NS115608. We would like to thank the Genetically-Encoded Neuronal Indicator and Effector (GENIE) Project and the Janelia Research Campus of the Howard Hughes Medical Institute for generously allowing the use of GCaMP6 in our research. We would like to thank Dr. Yavin Shaham for critical reading of the manuscript.

AUTHOR CONTRIBUTIONS

B.L., L.Z., G.B., Y.L., C.G., and D.T.L. conceptualized the project. B.L., L.Z., and G.B. designed the experiments, constructed the experimental setup, and built the custom imaging system. L.Z. performed the majority of surgery and data acquisition, Y.Z. performed the remaining experiments. G.B. performed the initial exploratory data analysis. B.L. performed the majority of data analysis. R.C. performed the decoding analysis. C.T.W., N.J.B., A.J.D., Y.L., and C.G. contributed critical intellectual inputs throughout the project. D.T.L. supervised all aspects of the project. B.L. and D.T.L. wrote the manuscript with inputs from all other authors.

DECLARATION OF INTERESTS

The authors declare no competing interests

Received: March 1, 2022
Revised: March 8, 2022
Accepted: April 7, 2022
Published: May 20, 2022

REFERENCES

Barbera, G., Liang, B., Zhang, L., Gerfen, C.R., Culurciello, E., Chen, R., Li, Y., and Lin, D.T. (2016). Spatially compact neural clusters in the dorsal striatum encode locomotion relevant information. Neuron *92*, 202–213. https://doi.org/10.1016/j.neuron.2016.08.037.

Bartholomew, R.A., Li, H., Gaidis, E.J., Stackmann, M., Shoemaker, C.T., Rossi, M.A., and Yin, H.H. (2016). Striatonigral control of movement velocity in mice. Eur. J. Neurosci. *43*, 1097–1110. https://doi.org/10.1111/ejn.13187.

Bolam, J., Hanley, J., Booth, P., and Bevan, M. (2000). Synaptic organisation of the basal ganglia. J. Anat. *196*, 527–542.

Burke, D.A., Rotstein, H.G., and Alvarez, V.A. (2017). Striatal local circuitry: a new framework for lateral inhibition. Neuron *96*, 267–284. https://doi.org/10.1016/j.neuron.2017.09.019.

Cao, V.Y., Ye, Y., Mastwal, S., Ren, M., Coon, M., Liu, Q., Costa, R.M., and Wang, K.H. (2015). Motor learning consolidates arc-expressing neuronal ensembles in secondary motor cortex. Neuron *86*, 1385–1392. https://doi.org/10.1016/j.neuron.2015.05.022.

Carelli, R.M., Wolske, M., and West, M.O. (1997). Loss of lever press-related firing of rat striatal forelimb neurons after repeated sessions in a lever pressing task. J. Neurosci. *17*, 1804–1814.

Chen, T.W., Wardill, T.J., Sun, Y., Pulver, S.R., Renninger, S.L., Baohan, A., Schreiter, E.R., Kerr, R.A., Orger, M.B., Jayaraman, V., et al. (2013). Ultrasensitive fluorescent proteins for imaging neuronal activity. Nature *499*, 295–300. https://doi.org/10.1038/nature12354.

Cho, J., and West, M.O. (1997). Distributions of single neurons related to body parts in the lateral striatum of the rat. Brain Res. *756*, 241–246. https://doi.org/10.1016/s0006-8993(97)00143-1.

Coffey, K.R., Nader, M., and West, M.O. (2016). Single body parts are processed by individual neurons in the mouse dorsolateral striatum. Brain Res. *1636*, 200–207.

Coffey, K.R., Nader, M., Bawa, J., and West, M.O. (2017). Homogeneous processing in the striatal direct and indirect pathways: single body part sensitive type II b neurons may express either dopamine receptor D1 or D2. Eur. J. Neurosci. *46*, 2380–2391.

Costa, R.M., Cohen, D., and Nicolelis, M.A. (2004). Differential corticostriatal plasticity during fast and slow motor skill learning in mice. Curr. Biol. *14*, 1124–1134. https://doi.org/10.1016/j.cub.2004.06.053.

Cui, G., Jun, S.B., Jin, X., Pham, M.D., Vogel, S.S., Lovinger, D.M., and Costa, R.M. (2013). Concurrent activation of striatal direct and indirect pathways during action initiation. Nature *494*, 238–242. https://doi.org/10.1038/nature11846.

da Silva, J.A., Tecuapetla, F., Paixao, V., and Costa, R.M. (2018). Dopamine neuron activity before action initiation gates and invigorates future movements. Nature *554*, 244. https://doi.org/10.1038/nature25457.

Dobbs, L.K., Kaplan, A.R., Lemos, J.C., Matsui, A., Rubinstein, M., and Alvarez, V.A. (2016). Dopamine regulation of lateral inhibition between striatal neurons gates the stimulant actions of cocaine. Neuron *90*, 1100–1113. https://doi.org/10.1016/j.neuron.2016.04.031.

Fobbs, W.C., Bariselli, S., Licholai, J.A., Miyazaki, N.L., Matikainen-Ankney, B.A., Creed, M.C., and Kravitz, A.V. (2020). Continuous representations of speed by striatal medium spiny neurons. J. Neurosci. *40*, 1679–1688. https://doi.org/10.1523/JNEUROSCI.1407-19.2020.

Friedman, J.H. (2002). Stochastic gradient boosting. Comput. Stat. Data. *38*, 367–378. https://doi.org/10.1016/S0167-9473(01)00065-2.

Geddes, C.E., Li, H., and Jin, X. (2018). Optogenetic editing reveals the hierarchical organization of learned action sequences. Cell *174*, 32–43.e15. https://doi.org/10.1016/j.cell.2018.06.012.

Gerfen, C.R., Engber, T.M., Mahan, L.C., Susel, Z., Chase, T.N., Monsma, F.J., Jr., and Sibley, D.R. (1990). D1 and D2 dopamine receptor-regulated gene expression of striatonigral and striatopallidal neurons. Science *250*, 1429–1432.

Giovannucci, A., Friedrich, J., Gunn, P., Kalfon, J., Brown, B.L., Koay, S.A., Taxidis, J., Najafi, F., Gauthier, J.L., and Zhou, P. (2019). CaImAn an open source tool for scalable calcium imaging data analysis. Elife *8*, e38173.

Gittis, A.H., Leventhal, D.K., Fensterheim, B.A., Pettibone, J.R., Berke, J.D., and Kreitzer, A.C. (2011). Selective inhibition of striatal fast-spiking interneurons causes dyskinesias. J. Neurosci. *31*, 15727–15731. https://doi.org/10.1523/JNEUROSCI.3875-11.2011.

Gritton, H.J., Howe, W.M., Romano, M.F., DiFeliceantonio, A.G., Kramer, M.A., Saligrama, V., Bucklin, M.E., Zemel, D., and Han, X. (2019). Unique contributions of parvalbumin and cholinergic interneurons in organizing striatal networks during movement. Nat. Neurosci. *22*, 586–597. https://doi.org/10.1038/s41593-019-0341-3.

Haber, S.N., Fudge, J.L., and McFarland, N.R. (2000). Striatonigrostriatal pathways in primates form an ascending spiral from the shell to the dorsolateral striatum. J. Neurosci. *20*, 2369–2382.

Howe, M.W., and Dombeck, D.A. (2016). Rapid signalling in distinct dopaminergic axons during locomotion and reward. Nature *535*, 505–510. https://doi.org/10.1038/nature18942.

Jin, X., Tecuapetla, F., and Costa, R.M. (2014). Basal ganglia subcircuits distinctively encode the parsing and concatenation of action sequences. Nat. Neurosci. *17*, 423–430. https://doi.org/10.1038/nn.3632.

Jones, B.J., and Roberts, D.J. (1968). The quantitative measurement of motor inco-ordination in naive mice using an accelerating rotarod. J. Pharm. Pharmacol. *20*, 302–304. https://doi.org/10.1111/j.2042-7158.1968.tb09743.x.

Kim, N., Barter, J.W., Sukharnikova, T., and Yin, H.H. (2014). Striatal firing rate reflects head movement velocity. Eur. J. Neurosci. *40*, 3481–3490. https://doi.org/10.1111/ejn.12722.

Klaus, A., Martins, G.J., Paixao, V.B., Zhou, P., Paninski, L., and Costa, R.M. (2017). The spatiotemporal organization of the striatum encodes action space. Neuron *95*, 1171–1180.e7. https://doi.org/10.1016/j.neuron.2017.08.015.

Kravitz, A.V., Freeze, B.S., Parker, P.R.L., Kay, K., Thwin, M.T., Deisseroth, K., and Kreitzer, A.C. (2010). Regulation of parkinsonian motor behaviours by optogenetic control of basal ganglia circuitry. Nature *466*, U622–U627. https://doi.org/10.1038/nature09159.

Kupferschmidt, D.A., Juczewski, K., Cui, G., Johnson, K.A., and Lovinger, D.M. (2017). Parallel, but dissociable, processing in discrete corticostriatal inputs encodes skill learning. Neuron *96*, 476–489.e5. https://doi.org/10.1016/j.neuron.2017.09.040.

Lalonde, R., Bensoula, A., and Filali, M. (1995). Rotorod sensorimotor learning in cerebellar mutant mice. Neurosci. Res. *22*, 423–426.

Lee, K., Holley, S.M., Shobe, J.L., Chong, N.C., Cepeda, C., Levine, M.S., and Masmanidis, S.C. (2017). Parvalbumin interneurons modulate striatal output and enhance performance during associative learning. Neuron *93*, 1451–1463.e4. https://doi.org/10.1016/j.neuron.2017.02.033.

Liang, B., Zhang, L., Barbera, G., Fang, W., Zhang, J., Chen, X., Chen, R., Li, Y., and Lin, D.T. (2018). Distinct and dynamic ON and OFF neural ensembles in the prefrontal cortex code social exploration. Neuron *100*, 700–714.e9. https://doi.org/10.1016/j.neuron.2018.08.043.

Liang, B., Zhang, L., Moffitt, C., Li, Y., and Lin, D.T. (2019). An open-source automated surgical instrument for microendoscope implantation. J. Neurosci. Methods *311*, 83–88. https://doi.org/10.1016/j.jneumeth.2018.10.013.

Martiros, N., Burgess, A.A., and Graybiel, A.M. (2018). Inversely active striatal projection neurons and interneurons selectively delimit useful behavioral sequences. Curr. Biol. *28*, 560–573.e5. https://doi.org/10.1016/j.cub.2018.01.031.

Mittler, T., Cho, J., Peoples, L.L., and West, M.O. (1994). Representation of the body in the lateral striatum of the freely moving rat: single neurons related to licking. Exp. Brain Res. *98*, 163–167. https://doi.org/10.1007/BF00229122.

Nonomura, S., Nishizawa, K., Sakai, Y., Kawaguchi, Y., Kato, S., Uchigashima, M., Watanabe, M., Yamanaka, K., Enomoto, K., Chiken, S., et al. (2018). Monitoring and updating of action selection for goal-directed behavior through the striatal direct and indirect pathways. Neuron *99*, 1302–1314.e5. https://doi.org/10.1016/j.neuron.2018.08.002.

O'Hare, J.K., Li, H., Kim, N., Gaidis, E., Ade, K., Beck, J., Yin, H., and Calakos, N. (2017). Striatal fast-spiking interneurons selectively modulate circuit output and are required for habitual behavior. Elife *6*, e26231. https://doi.org/10.7554/eLife.26231.

Owen, S.F., Berke, J.D., and Kreitzer, A.C. (2018). Fast-spiking interneurons supply feedforward control of bursting, calcium, and plasticity for efficient learning. Cell *172*, 683–695.e5. https://doi.org/10.1016/j.cell.2018.01.005.

Panigrahi, B., Martin, K.A., Li, Y., Graves, A.R., Vollmer, A., Olson, L., Mensh, B.D., Karpova, A.Y., and Dudman, J.T. (2015). Dopamine is required for the neural representation and control of movement vigor. Cell *162*, 1418–1430. https://doi.org/10.1016/j.cell.2015.08.014.

Parker, J.G., Marshall, J.D., Ahanonu, B., Wu, Y.W., Kim, T.H., Grewe, B.F., Zhang, Y., Li, J.Z., Ding, J.B., Ehlers, M.D., and Schnitzer, M.J. (2018). Diametric neural ensemble dynamics in parkinsonian and dyskinetic states. Nature *557*, 177–182. https://doi.org/10.1038/s41586-018-0090-6.

Planert, H., Szydlowski, S.N., Hjorth, J.J., Grillner, S., and Silberberg, G. (2010). Dynamics of synaptic transmission between fast-spiking interneurons and striatal projection neurons of the direct and indirect pathways. J. Neurosci. *30*, 3499–3507. https://doi.org/10.1523/JNEUROSCI.5139-09.2010.

Pnevmatikakis, E.A., and Giovannucci, A. (2017). NoRMCorre: an online algorithm for piecewise rigid motion correction of calcium imaging data. J. Neurosci. Methods *291*, 83–94.

Pnevmatikakis, E.A., Soudry, D., Gao, Y., Machado, T.A., Merel, J., Pfau, D., Reardon, T., Mu, Y., Lacefield, C., and Yang, W. (2016). Simultaneous denoising, deconvolution, and demixing of calcium imaging data. Neuron *89*, 285–299.

Richie, C.T., Whitaker, L.R., Whitaker, K.W., Necarsulmer, J., Baldwin, H.A., Zhang, Y., Fortuno, L., Hinkle, J.J., Koivula, P., Henderson, M.J., et al. (2017). Near-infrared fluorescent protein iRFP713 as a reporter protein for optogenetic vectors, a transgenic Cre-reporter rat, and other neuronal studies. J. Neurosci. Methods *284*, 1–14. https://doi.org/10.1016/j.jneumeth.2017.03.020.

Rueda-Orozco, P.E., and Robbe, D. (2015). The striatum multiplexes contextual and kinematic information to constrain motor habits execution. Nat. Neurosci. *18*, 453–460. https://doi.org/10.1038/nn.3924.

Sales-Carbonell, C., Taouali, W., Khalki, L., Pasquet, M.O., Petit, L.F., Moreau, T., Rueda-Orozco, P.E., and Robbe, D. (2018). No discrete start/stop signals in the dorsal striatum of mice performing a learned action. Curr. Biol. *28*, 3044–3055.e5. https://doi.org/10.1016/j.cub.2018.07.038.

Santos, F.J., Oliveira, R.F., Jin, X., and Costa, R.M. (2015). Corticostriatal dynamics encode the refinement of specific behavioral variability during skill learning. Elife *4*, e09423. https://doi.org/10.7554/eLife.09423.

Sheintuch, L., Rubin, A., Brande-Eilat, N., Geva, N., Sadeh, N., Pinchasof, O., and Ziv, Y. (2017). Tracking the same neurons across multiple days in Ca^{2+} imaging data. Cell Rep. *21*, 1102–1115. https://doi.org/10.1016/j.celrep.2017.10.013.

Sheng, M.-j., Lu, D., Shen, Z.-m., and Poo, M.-m. (2019). Emergence of stable striatal D1R and D2R neuronal ensembles with distinct firing sequence during motor learning. Proc. Natl. Acad. Sci. U S A *116*, 11038. https://doi.org/10.1073/pnas.1901712116.

Shin, J.H., Kim, D., and Jung, M.W. (2018). Differential coding of reward and movement information in the dorsomedial striatal direct and indirect pathways. Nat. Commun. *9*, 404. https://doi.org/10.1038/s41467-017-02817-1.

Tang, C., Pawlak, A.P., Prokopenko, V., and West, M.O. (2007). Changes in activity of the striatum during formation of a motor habit. Eur. J. Neurosci. *25*, 1212–1227. https://doi.org/10.1111/j.1460-9568.2007.05353.x.

Tang, C.C., Root, D.H., Duke, D.C., Zhu, Y., Teixeria, K., Ma, S., Barker, D.J., and West, M.O. (2009). Decreased firing of striatal neurons related to licking during acquisition and overtraining of a licking task. J. Neurosci. *29*, 13952–13961. https://doi.org/10.1523/JNEUROSCI.2824-09.2009.

Taverna, S., Ilijic, E., and Surmeier, D.J. (2008). Recurrent collateral connections of striatal medium spiny neurons are disrupted in models of Parkinson's disease. J. Neurosci. *28*, 5504–5512. https://doi.org/10.1523/JNEUROSCI.5493-07.2008.

Tecuapetla, F., Matias, S., Dugue, G.P., Mainen, Z.F., and Costa, R.M. (2014). Balanced activity in basal ganglia projection pathways is critical for contraversive movements. Nat. Commun. *5*, 4315. https://doi.org/10.1038/ncomms5315.

Xiao, L., Bornmann, C., Hatstatt-Burkle, L., and Scheiffele, P. (2018). Regulation of striatal cells and goal-directed behavior by cerebellar outputs. Nat. Commun. *9*. ARTN 3133. https://doi.org/10.1038/s41467-018-05565-y.

Yin, H.H., Mulcare, S.P., Hilario, M.R., Clouse, E., Holloway, T., Davis, M.I., Hansson, A.C., Lovinger, D.M., and Costa, R.M. (2009). Dynamic reorganization of striatal circuits during the acquisition and consolidation of a skill. Nat.

Neurosci. *12*, 333–341. https://doi.org/10.1038/nn.2261.

Yttri, E.A., and Dudman, J.T. (2016). Opponent and bidirectional control of movement velocity in the basal ganglia. Nature *533*, 402–406. https://doi.org/10.1038/nature17639.

Zhang, L., Liang, B., Barbera, G., Hawes, S., Zhang, Y., Stump, K., Baum, I., Yang, Y., Li, Y., and Lin, D.T. (2019). Miniscope GRIN lens system for calcium imaging of neuronal activity from deep brain structures in behaving animals. Curr. Protoc. Neurosci. *86*, e56. https://doi.org/10.1002/cpns.56.

Zhou, P., Resendez, S.L., Rodriguez-Romaguera, J., Jimenez, J.C., Neufeld, S.Q., Giovannucci, A., Friedrich, J., Pnevmatikakis, E.A., Stuber, G.D., and Hen, R. (2018). Efficient and accurate extraction of in vivo calcium signals from microendoscopic video data. Elife *7*, e28728.

STAR★METHODS

KEY RESOURCES TABLE

REAGENT or RESOURCE	SOURCE	IDENTIFIER
Bacterial and virus strains		
AAV1.CAG.Flex.GCaMP6s.WPRE.SV40	UPenn Vector Core	CS0705-3CS
AAV1-EF1α-DIO-eNpHR3.0-EYFP	UPenn Vector Core	CS1014
AAV1-EF1a-DIO-EYFP	UPenn Vector Core	CS1012-3CS
Experimental models: Organisms/strains		
C57BL/6J congenic, D1-Cre, FK150 line	Gensat	RRID:MMRRC_036916-UCD
C57BL/6J congenic, D2-Cre, ER44 line	Gensat	RRID:MMRRC_032108-UCD
Software and algorithms		
Matlab	Mathworks	http://www.mathworks.com
Graphpad Prism	Graphpad	https://www.graphpad.com/
CaImAn-Matlab toolbox	Giovannucci et al. (2019)	https://github.com/flatironinstitute/CaImAn-MATLAB
Custom MATLAB scripts for data analysis	This work	N/A
Other		
Miniature microscope for *in vivo* calcium imaging	Barbera et al. (2016); Zhang et al. (2019)	https://doi.org/10.5281/zenodo.5710817
Dual LED miniScope prototype	This work	https://zenodo.org/badge/latestdoi/467669999
Automated surgical instrument for GRIN lens implantation	Liang et al. (2019)	https://doi.org/10.5281/zenodo.5710828

RESOURCE AVAILABILITY

Lead contact

Further information and requests for resources and reagents should be directed to and will be fulfilled by the lead contact, Dr. Da-Ting Lin (da-ting.lin@nih.gov)

Materials availability

This study did not generate new unique reagents

Data and code availability

- All data reported in this paper will be shared by the lead contact upon request.
- This paper does not report original code. All custom MATLAB scripts will be available upon request.
- Any additional information required to reanalyze the data reported in this paper is available from the lead contact upon request.

EXPERIMENTAL MODEL AND SUBJECT DETAILS

All experiments were conducted in accordance with the guidelines of Institutional Animal Care and Use Committee, the Intramural Research Program, National Institute on Drug Abuse, National Institutes of Health. Transgenic mice expressing Cre recombinase under the control of the dopamine D1 receptor (D1-Cre, FK150 line, C57BL/6J congenic, Gensat, RRID:MMRRC_036916-UCD) or dopamine D2 receptor (D2-Cre, ER44 line, C57BL/6J congenic, Gensat, RRID:MMRRC_032108-UCD) were used in the

experiments. All mice were male at 3–4 months of age and 25–30 g. All mice were maintained in a regular light cycle (7:00am–7:00 pm) and provided with food and water *ad libitum*.

METHOD DETAILS

Virus injection

For calcium imaging experiments, D1-Cre and D2-Cre mice were stereotaxically injected with a Cre-inducible adeno-associated virus (AAV) expressing GCaMP6s (AAV1.CAG.Flex.GCaMP6s. WPRE.SV40; 500 nL; University of Pennsylvania Vector Core). AAV was injected into the right hemisphere of the dorsal striatum for each mouse using the target stereotactic coordinates: AP: +0.8 mm, ML: −1.8 mm, DV: -3 mm. Perpendicular injections would cause scar tissue in the corpus callosum, which was difficult to remove during GRIN lens implantation, and so we chose to inject the virus from cranial surface coordinate of AP: −0.93, ML: −1.8, with a 30° angle shift caudally, going into with a depth of 3.46 mm. For combined imaging/optogenetic inhibition, AAV1. syn.Flex.GCaMP7f (Addgene) was mixed with AAV1.EF1a.DIO.eNpHR3.0-iRFP (packaged by Vigene) before injection. AAV was injected into the right hemisphere of the dorsal striatum for each mouse using the target stereotactic coordinates: AP: +0.8 mm, ML: −1.8 mm, DV: -3 mm. Because perpendicular injection would cause scar tissue in the corpus callosum, which was difficult to remove during GRIN lens implantation, we chose to inject the virus from cranial surface coordinate of AP: −0.93, ML: −1.8, with a 30° angle shift caudally, going into with a depth of 3.46 mm. For optogenetic experiments, D1-Cre and D2-Cre mice were stereotaxically injected with a Cre-inducible AAV carrying Halorhodopsin (AAV1-EF1α-DIO-eNpHR3.0-EYFP; 1μL/side; University of Pennsylvania Vector Core) or EYFP (control; AAV1-EF1a-DIO-EYFP; 1μL/side; University of Pennsylvania Vector Core). The AAV was bilaterally injected into the dorsal striatum for each mouse using the stereotactic coordinates: +0.9 mm A/P, ±2 mm M/L, and −2.7 mm D/V. Before the viral injection, mice were anaesthetized with 2% isoflurane in oxygen at a flow rate of 0.4 L/min and mounted on a stereotactic frame (Model 962, David Kopf Instruments). Mice body temperatures were maintained at 37°C using a temperature control system (TCAT-2DF, Physitemp). Sterile ocular lubricant ointment (Dechra Veterinary Products) was applied to mouse corneas to prevent drying. Mouse scalp fur was shaved, and mouse skin was cleaned with 7.5% betadine and 70% alcohol. A hole was drilled at the injection site using a 0.5-mm diameter round burr on a high-speed rotary micro drill (19007–05, Fine Science Tools). Virus solution was injected at a rate of 25 nL/min using a micro pump and Micro4 controller (World Precision Instruments). After injection, the injection needle was kept in the parenchyma for 5 min before being slowly withdrawn. Then skin was sutured. Mice were returned to their home cage to recover from anesthesia in a 37°C isothermal chamber (Lyon Technologies, Inc).

GRIN lens and optical fiber implantation

For calcium imaging experiments, one or two weeks after AAV injection, a 1-mm diameter GRIN lens (GRINTECH; NEM-100-25-10-860-S) was directly implanted into the dorsal striatum using similar procedure as previously described (Barbera et al., 2016). A detailed surgical procedure can be found in our previous publication (Zhang et al., 2019). In brief, mice were anesthetized with ketamine/xylazine (ketamine: 100 mg/kg and xylazine: 15 mg/kg). A round section of dorsal scalp was excised and a 1.1 mm-diameter craniotomy was made at the stereotactic coordinates (A/P: +0.9 mm. M/L: +1.8 mm). Before GRIN lens implantation, brain tissue above the dorsal striatum was aspirated using a vacuum through a 30-gauge blunt-end needle. The needle was attached to a custom-constructed motorized stereotaxic instrument controlled by a MATLAB-based software (Liang et al., 2019). The GRIN lens was then lowered into dorsal striatum. Melted agarose (1%, melted in microwave, maintained in 40°C water bath) was applied onto the skull around the GRIN lens to seal the gap, and the GRIN lens was cemented in place with dental acrylic (Metabond S380, Parkell).

For optogenetic experiments, following the virus injection (two weeks), optical fibers (200-μm core diameter, 0.39 NA; Thorlabs, FT200EMT), constructed as previously described with minor modifications (da Silva et al., 2018) were lowered to above virus injection sites (AP: +0.9 mm, M/L: ±2 mm, D/V: −2.1 mm) and cemented in place with dental acrylic (Metabond S380, Parkell). After the implantation surgery, mice were returned to their home cage to recover from anesthesia in a 37°C isothermal chamber (Lyon Technologies, Inc).

Rotarod tasks

For calcium imaging experiments, we conducted two rotarod tasks using two batches of mice with a standard mouse rotarod apparatus (Ugo Basile, 47650). D1-Cre (n = 9) and D2-Cre (n = 6) mice were trained in

an accelerating rotarod task similar to previously described (Yin et al., 2009). Mice were trained in 8 sessions on alternate days for 15 days in total. For each session, there were 10 trials and mice were allowed to rest for 5 min between trials. The mice initially ran on the rotarod at a speed of 4 resolutions per minute (rpm) for approximately 10 s. The rotarod then accelerated from 4 to 40 rpms over 5 min for each trial. The trial was ended if mice fell off the rod, started rotating with the rod, or successfully stayed on rod for the full 300 s. The behavioral performance (latency to fall) was quantified by the temporal interval between the acceleration onset and the end of the trial (Figure 1B). For optogenetic experiments, mice were trained as described above for the first calcium imaging experiment.

Calcium imaging using miniature microscope

Miniature fluorescence microscope (miniScope) was used for calcium imaging. Detailed information about the miniScope can be found in our previous study (Barbera et al., 2016; Liang et al., 2018; Zhang et al., 2019). Design files and part list can be found in the Github repository (https://github.com/giovannibarbera/miniscope_v1.0). The miniScope consists of a blue LED (465 nm XLamp XP-E, Cree), a filter set (excitation filter, ET470/40, Chroma; dichroic mirror, FF495, Semrock; emission filter, EM525/50, Chroma), relay optics (#83–605, #63–690, Edmund optics) and a CMOS sensor (MT9V022, Onsemi). The miniScope housing was 3D printed (SLArmor Nickel- NanoTool, Proto Labs). The LED power was set to 0.1–0.3 mW at the focal plane. The image size was 400 × 400 pixels, acquired at a frame rate of 10 Hz.

Three to eight weeks after the GRIN lens implantation, the miniScope with a detachable base was mounted on the mouse head. MiniScope was held by motorized translation stages (MTS50-Z8, Thorlabs) and lowered towards the GRIN lens while acquiring calcium images. After achieving the in-focus position, the base of the miniScope was cemented in place with dental acrylic (Metabond S380, Parkell), and the main body of the miniScope was detached from the base. Before calcium imaging experiment, the main body of the miniScope was re-mounted and secured to the base on the mouse head through a side-locking screw. Mice were then returned to home cage for 30- minute recovery before the rotarod tasks. Mouse behavior was also recorded using a color camera (Blackfly, FLIR), which was synchronized with miniScope recordings using a TTL (Transistor-Transistor Logic) signal from the miniScope controller. Behavior videos were used to determine the acceleration onset and the end of the trial.

Combined calcium imaging and optogenetics using dual LED miniScope prototype

For the Dual LED miniScope prototype, main imaging path configuration is the same as described above except that the main dichroic is a dual band (Chroma Technology 59022×), on the excitation light path, we used a dichoric mirror (T495lpxr, Chroma) to combine the blue LED and the lime LED (566–569 nm peak wavelength, Lumileds). We placed an excitation filter in front of each LED (ET470/40× for blue LED, ET570/20× for lime LED, both from Chroma). The line LED power measure at the bottom of miniScope prototype was approximately 60 μW.

Optogenetic experiments

Optogenetic inhibition was delivered with a 568-nm laser (Sapphire LP, Coherent). The laser through fiber-optic cable was coupled with a rotatory joint and a branching fiber-optic patch cord (Doric lens). The laser power at fiber optics tip of each branch was ~10 mW, much higher than the lime LED power (60 μW) used in the combined calcium imaging and optogenetic experiment described above. We conducted two types of optogenetic inhibition: early inhibition and late inhibition for D1-Cre and D2-Cre mice (four groups in total). For early-inhibition experiment, the laser was turned on for the early stage of the trial (90 s for session 1 and 120 s for the rest of the sessions) from the acceleration onset. For late-inhibition experiment, the laser was turned on after the early stage of the trial (90 s for session 1 and 120 s for the rest of the sessions) from the acceleration onset until the end of the trial.

Immunostaining

At the end of entire experiments, mice were anesthetized with an overdose of ketamine (150 mg/kg) and xylazine (22.5 mg/kg), perfused with phosphate buffer solution (PBS) first and followed by a fixation buffer containing 4% paraformaldehyde (PFA) in PBS. Mice brains were dissected and post-fixed with 4% PFA in PBS overnight at 4°C. Fixed brains were sectioned via a Vibratome (Leica, VT1000S) and 30 μm coronal brain slices were collected. Slices were then mounted and counterstained with DAPI (Thermo Fisher Scientific,

D1306) and covered with coverslip. Fluorescent images were obtained through an Olympus VS120 scanner and analyzed using ImageJ (NIH).

Calcium image processing

Calcium images were processed and analyzed using scripts in MATLAB (Mathworks). Calcium images were first stabilized using motion correction toolbox NoRMCorre (Pnevmatikakis and Giovannucci, 2017). Constrained non-negative matrix factorization-based calcium image processing toolbox CaImAn-MATLAB (Giovannucci et al., 2019; Pnevmatikakis et al., 2016; Zhou et al., 2018) was used to extract calcium signals. We manually added additional seeds as necessary based on the correlation image calculated by the correlation of neighboring pixels of calcium images. For each session, images of 10 trials were concatenated and temporally sub-sampled to half for calcium signal extraction. The calcium trace (ΔF/F) was set to zero if the value was below 3× baseline noise level, and ΔF/F was then normalized by ΔF/F/max (ΔF/F) for further data analysis. For each session, a global cell map was generated, including all the extracted neurons in that session, with a neuron denoted as active in one trial if it displayed calcium transient above 3× baseline noise level. Subsequently the active cell number in each trial of each session was calculated (Figure 1E).

Cell registration across days

To register the spatial footprints of neurons identified across different sessions, the displacement fields of the correlation image among sessions were first calculated using

MATLAB function (*imregdemons*) to estimate the shift owing to the remounting of the miniscope and slow shift between the brain tissue and GRIN lens over time. The displacement fields were then applied to cell spatial footprints to align the rest of the sessions to the first session. Cell registration toolbox CellReg (Sheintuch et al., 2017) was then used for cell registration. Both distance model and spatial footprint model were used. Instead of correlation coefficient as a measurement of spatial footprint similarity (Sheintuch et al., 2017), cosine similarity was used in our data. Pair-wised cell-cell distance and spatial footprint similarity was calculated from all recording sessions of all mice to decide the threshold of whether two cells in different sessions were the same or not. Psame of 0.5 was used to choose the threshold (Sheintuch et al., 2017). The cell with the highest spatial footprint similarity was chosen as the cell pair (same cell) if there were multiple cells that were above the threshold. Cell-to-cell mapping indices were then generated to indicate the relationship of the cell identity among sessions, which were used in cell overlap analyses in Figure 2.

QUANTIFICATION AND STATISTICAL ANALYSIS

Data analysis

Cell overlap analysis

Cell overlap was calculated to evaluate the similarity of the different neuron ensembles (i.e., early- and late-stage neurons in Figure 2) among different trials (or sessions). For within-session cell overlap, trial-to-trial pairwise cell overlaps (45 pairs) were first calculated using the Sørensen–Dice index: $2 \cdot NA \cap B/(NA + NB)$, where $NA \cap B$ is the cell number of intersect between trial A and trial B, NA is the cell number in trial A and NB is the cell number in trial B. The degree of overlap predicted by chance (Figures 2E–2J) was calculated by $2NANB/(N(NA + NB))$, where N is the total imaged cell number in trial A and B (Liang et al., 2018). The average of all trial-to-trial cell overlaps (45 pairs) was then used as the within-session cell overlap for a given session. Similarly, cross-session cell overlap, trial-to-trial pairwise cell overlaps (100 pairs) were first calculated using the Sørensen–Dice index and the average of all trial-to-trial cell overlaps (100 pairs) was used as the cross-session cell overlap for a given session-session pair. And chance-level cross-session overlaps were also calculated.

Identification of intratrial early- and late-stage neurons in accelerating rotarod task

For each neuron, the activity-speed correlation was calculated using Spearman's correlation coefficient (SCC) between the calcium activity and rotarod speed using 10-s bins (100 frames). The calcium activity was the normalized calcium traces as described in above Calcium image processing section. For each bin, the activity was the average of the normalized ΔF/F. A given neuron was identified as intratrial late-stage neuron if the SCC of activity-speed correlation was significant ($p < 0.05$) and positive, and a neuron was identified as intratrial early-stage neuron if the SCC of activity-speed correlation was significant and negative. The percentage of intratrial late-stage neurons and intratrial early-stage neurons per trial were

then calculated. For each mouse, Pearson's correlation coefficient between behavioral performance (latency to fall) and cell percentage of late-stage (and early- stage) neurons was calculated.

Speed decoding

Gradient boosting machine (GBM) algorithm (Friedman, 2002) was used for speed decoding (Figures 3C and 3D). GBM was implemented in R with the gbm and plyr packages (https://cran.r-project.org/). GBM iteratively added basis functions in a greedy fashion to reduce the root mean square loss function. The base learner was a tree model and parameters were tuned by using internal cross-validation. The GBM model was evaluated using ten-folder cross-validation. The decoding performance was measured by the Pearson's correlation coefficient between predicted value and observed value (Figure 3D).

Statistics

All reported sample numbers represented biological replicates. All data were presented as mean ± SEM unless otherwise specified. In all the figures, * $p < 0.05$; ** $p < 0.01$; *** $p < 0.001$; **** $p < 0.0001$; ns represented not significant ($p > 0.05$). All statistical analyses were performed using Graphpad Prism (Graphpad) or MATLAB (Mathworks). Non-parametric tests were used in all statistical analysis except optogenetic data (Figure 4) where we used a two-way ANOVA with Sidak's multiple comparisons post-hoc test applied when appropriate. All tests were two-tailed, and statistical significance was defined as $p < 0.05$.

Sample size estimation

Our estimates of animal use for *in vivo* calcium imaging and optogenetic experiment was based on past experiences and those presented in the literature(Barbera et al., 2016; Klaus et al., 2017; Parker et al., 2018).